The 5th International Symposium - Supercritical CO2 Power Cycles
March 28-31, 2016, San Antonio, Texas

Multi-Scale Coupled Physics Models and Experiments for Performance and Life Prediction of Supercritical CO2 Turbomachinery Components

Azam Thatte*, Adrian Loghin, Etienne Martin, Voramon Dheeradhada,

Youngwon Shin, Balajee Ananthasayanam

General Electric Company, GE Global Research, One Research Circle, Niskayuna, NY 12309 USA.

* Corresponding author.

ABSTRACT

Component design, maturation and material development for sCO2 turbomachines in the 10MW to 500 MW range have been identified to be in the critical path for the successful implementation sCO2 power plants. However, the performance and life limiting mechanisms of these components in high pressure, high temperature sCO2 environment are not well understood. These mechanisms are governed by multi-scale coupled physics interactions combined with strong perturbations in performance variables around the critical point. In this paper, some of the work done by GE, under U.S. DOE PREDICTS program, in developing performance and life prediction models for Hybrid Gas Bearing (HGB) and Dry Gas Seal (DGS) is presented. From a system perspective, HGB can provide substantial benefits (~3 to 5%) to the modular CSP operation, while use of DGS limits the leakage losses (~2-3% improvement in cycle efficiency for 10 MW scale) as well as the windage losses in the generator (increase in generator efficiency by ~8%). Multi-scale coupled physics models to predict dynamic performance of HGB and DGS are developed. The models try to capture sCO2 specific phenomena like sonic transitions, possibility of phase change, flow induced and rotordynamic instabilities and large perturbations in apparent heat transfer coefficients due to Leidenfrost effect. The output of performance model is fed into 3D fracture mechanics based life prediction framework. Test campaigns to characterize corrosion of Nickel base super alloys in sCO2 environment are conducted and chemical kinetics models are built. LCF behavior of Ni base super alloys in high pressure, high temperature sCO2 is also being investigated using a novel experimental setup. Bayesian hybrid probabilistic models are developed to quantify uncertainty in multi-physics models and to validate models with statistical confidence. This strongly coupled performance and life prediction framework is a valuable tool to design a wide variety of sCO2 turbomachinery components and heat exchangers, analyze their performance in supercritical and trans-critical mission cycles and predict their life for long term durability of sCO2 turbomachines.

1. Introduction

U.S. Department of Energy (DOE) has recently sponsored research programs to develop megawatt scale supercritical CO2 (sCO2) turbine for use in concentrated solar power (CSP) and fossil based applications. GE in collaboration with Southwest Research Institute (SWRI) is leading this effort [1]. To achieve the CSP goal of $0.06/kW-hr LCOE and energy conversion efficiency > 50%, the sCO2 turbine relies critically on extremely low leakage film riding seals like dry gas seal (DGS). In addition, this seal is needed to protect the oil bearings of the sCO2 turbine from high temperature CO2 and also to avoid the windage losses in the generator resulting from possibility of ingress of highly viscous and dense supercritical CO2 (accounting to as much as 8% gain in generator efficiency). Although DGS technology has been used for O&G compressor applications, making it successful for stringent conditions of an sCO2 turbo-expander is challenging. Successful implementation of DGS technology in sCO2 turbo-expander would need the retirement of following key risks: (i) Abrupt phase change of CO2 from gas to liquid/ice as it passes through DGS could cause groove blockage leading to DGS failure (ii) LCF/ HCF in the springs due to cyclic compression under high temperature CO2. (iii) Dynamic instabilities due to choked/supersonic flow of CO2 leading to large perturbations in gas film stiffness and damping that can cause hard rubs and degradation in life (iv) Corrosion of the DGS-spring under high temperature CO2 environment. The effort in this paper is focused on addressing some of these risks through accurate coupled-physics based models. The output of DGS performance models serves as an input to the life prediction model in evaluating the durability of DGS under a typical sCO2 mission cycle.

From rotordynamics perspective, extremely high power densities associated with the sCO2 turbine and the long shaft of the turbine require mid-span support to achieve the high rotational speeds needed to meet turbine efficiency targets. One of the main challenges in doing so is that the traditional oil lubricated bearings cannot be located inside the working fluid pressure boundary (fluid temperatures much higher than oil evaporation temperatures). The mid-span bearings, if oil lubricated, need two sets of seals to isolate the working fluid from lubricating oil and represent a combined parasitic load of as much as 5% of the power plant output. These parasitic loads can be avoided by the use of hybrid gas bearing (HGB) which uses turbine working fluid itself as the lubricant for generating hydrostatic + hydrodynamic pressure and hence can operate in a high temperature, high pressure sCO2 environment without the use of oil lubrication or extra sealing. A successful and reliable implementation of HGB is expected to provide significant efficiency improvement in the sCO2 turbine for modular plants in 10MW scale. However, the behavior of hybrid gas bearing with supercritical CO2 as the working fluid has never been studied before and hence a careful investigation of its hydrodynamic and rotordynamic characteristics with perturbations associated with sCO2 fluid and sCO2 turbine is warranted.

2. Multiscale Coupled Physics Modeling Framework

Figure 1 shows the multi-scale coupled physics framework developed to study the performance and life of sCO2 turbomachinery components. Comprehensive fluid-structure-thermal interaction models for HGB and DGS are developed that provide the loading mission for these components in a typical sCO2 turbine field mission cycle. State of the art phase transition, 2 phase flow and thermal transport models are also developed. Models capture condensation, nucleate boiling and film boiling physics of CO2 and their effect on local temperature perturbations of turbomachines. Other components of the framework study corrosion, low cycle fatigue and fracture mechanics of Ni base superalloys in high pressure, high temperature sCO2 environment. A 3D fracture mechanics model is used to predict crack propagation rates in these Ni base superalloys under turbine mission cycle. A crack initiation model is also being developed that attempts to take into account oxidation, species diffusion and chemical kinetics of sCO2 in these alloys and predicts the crack initiation life. A novel method using high energy X-ray tomography is developed to capture 3D micro-crack evolution and propagation and to digitally reconstruct the crack topography for calibrating and validating the fracture mechanics model. Hybrid Bayesian probabilistic model is developed to encompass individual physics based models and experimental data into a coherent predictive framework and to quantify uncertainties in the model and to validate the models.

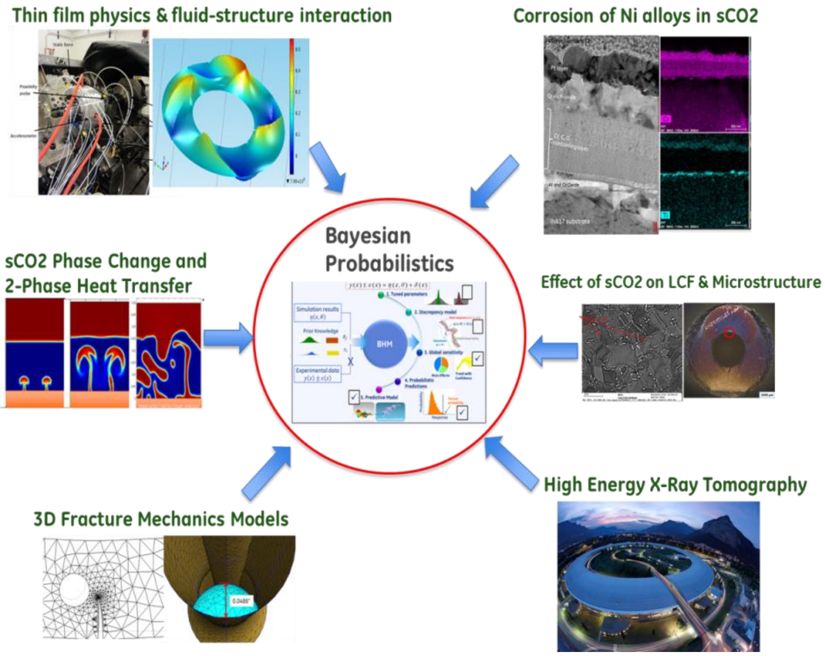

Figure 1: Multi-scale coupled physics performance and life prediction framework.

3. Dry Gas Seal Performance Model

Architecture of a 10 MWe sCO2 turboexpander rotor was presented in [1] where the DGS is mounted on the generator side and compressor side to separate the high pressure CO2 environment inside the turbine region from ambient air and from oil lubricated bearings. It also prevents the ingress of highly viscous and dense supercritical CO2 from entering generator and from causing excessive windage losses in the generator. Architecture of DGS used in 10 MWe sCO2 expander is presented in [14]. The stationary ring and rotating ring typically ride at a gap of 0.0001-0.0005 inch, hence allowing very little leakage. The transients in turbomachinery typically try to push the mating ring towards or pull away from the rotating ring with displacements that are several orders of magnitude larger than the running gap between primary and mating rings (~ 0.2 inch in current application). There is a balance of closing force exerted by spring and hydrostatic pressure and an opening force generated at the gap due to hydrodynamic pressure generation. The hydrodynamic force needs to act as a passive feedback mechanism and should try to maintain an equilibrium gap between stationary and rotating rings during rotor transients allowing for non-contact operation essential for longer life. It is important to analyze whether this in fact is the case for current design and loading mission of the sCO2 turboexpander in a CSP application. Authors have developed progressively higher fidelity models to study fluid-structure-thermal interactions occurring in DGS during operation in the sCO2 expander [14].

A lateral rotordynamic analysis was performed on the Sunshot turbine rotor in order to predict the high frequency vibratory loads seen by DGS, predict the DGS response to such loads and in turn predict the life of DGS under such loads. Figure 2 (a) shows the mode shapes for first four undamped critical speeds for the Sunshot rotor. Figure 2 (b) shows corresponding DGS performance model results. In (b) the top left image shows the hydrostatic + hydrodynamic pressure distribution in the thin sCO2 film between DGS rings. Top right image shows the radial velocity distribution in the sCO2 film. It can be seen that the radial velocity through the groove is in the radially inward direction as expected. Flow accelerates further radially inward as it exits the groove and moves towards the ID over the dam section. However an interesting phenomenon was observed in the ridge portion (region between adjacent grooves) of DGS. Here it can be seen that the radial velocity is in opposite direction, i.e. in radially outward direction over a region close to the groove end. This is most likely due to high flow resistance to pressure driven flow exhibited by extra-thin ridge portion of the surface. This radially outward component becomes negligible as we approach the OD. Such flow distributions help us understand the balance of local pressure forces and heat flow in thin CO2 film at DGS interface In (b), the bottom left image shows the Mach number distribution in the sCO2 film. In this particular case, even with very high circumferential and radial velocities the flow did not become choked. The reason for this is that the combination of large changes in pressure and temperature across DGS film cause large local density variations resulting in perturbations in speed of sound through the sCO2 film itself. In (b) the bottom right image shows the stress distribution in DGS rings obtained from coupled 3D fluid-structure-thermal interaction solution. More detailed description of this model and of DGS dynamic response to various vibratory mode shapes and to viscous shear induced perturbations is presented in [14].

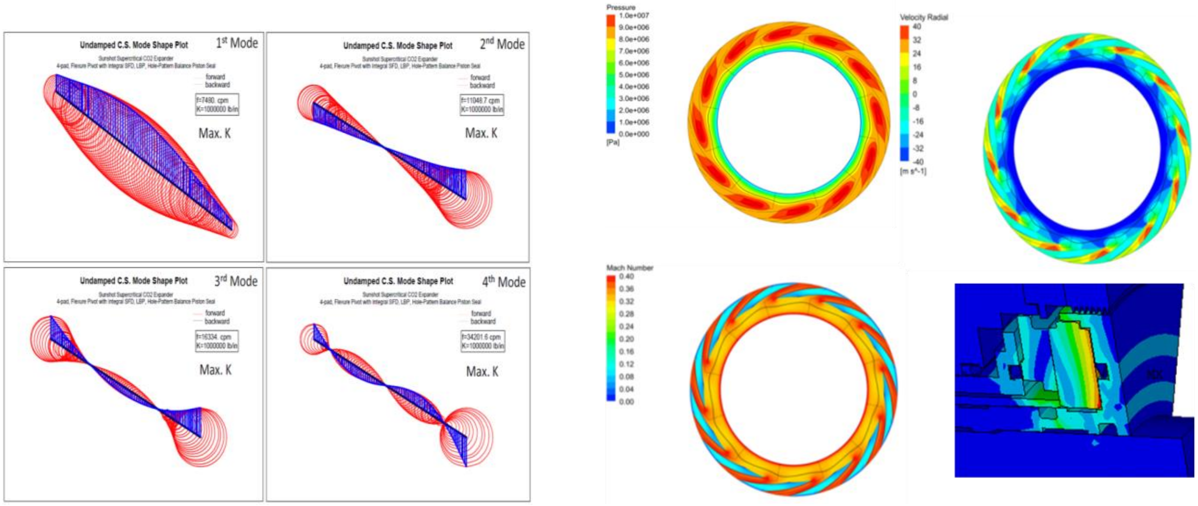

(a) (b)

Figure 2: (a) Mode shapes for first four undamped critical speeds for Sunshot rotor. (b) (To left): hydrostatic + hydrodynamic pressure distribution in the thin sCO2 film between DGS rings. (Top right): radial velocity distribution in the thin sCO2 film. (Bottom left): Mach number distribution in the thin sCO2 film. (Bottom right): stress distribution in DGS rings obtained from coupled 3D fluid-structure-thermal interaction.

Above DGS performance model establishes a limit on the amplitude of various modes of vibrations of DGS rotor ring (arising from axial transients, assembly tilt, thermal coning, waviness introduced by manufacturing tolerances) that can be tolerated without undergoing a dynamic rub event. This also guides the improvement in hydrostatic/ hydrodynamic film stiffness and damping characteristics of DGS. The results of the performance model feed into the DGS life prediction model.

Under the U.S. DOE PREDICTS program authors of this paper in collaboration with SWRI team will test the performance of the DGS system installed in a 10 MWe Sunshot sCO2 turbo-expander. The purpose of these tests is to study the key performance variables of DGS under steady state and transient CSP field conditions and validate the physics based models described above. Figure 3 (left) shows this 10MWe Sunshot turbine with the instrumented DGS. Figure 3(right) shows the DGS flow system designed to test the DGS performance in the turbine.

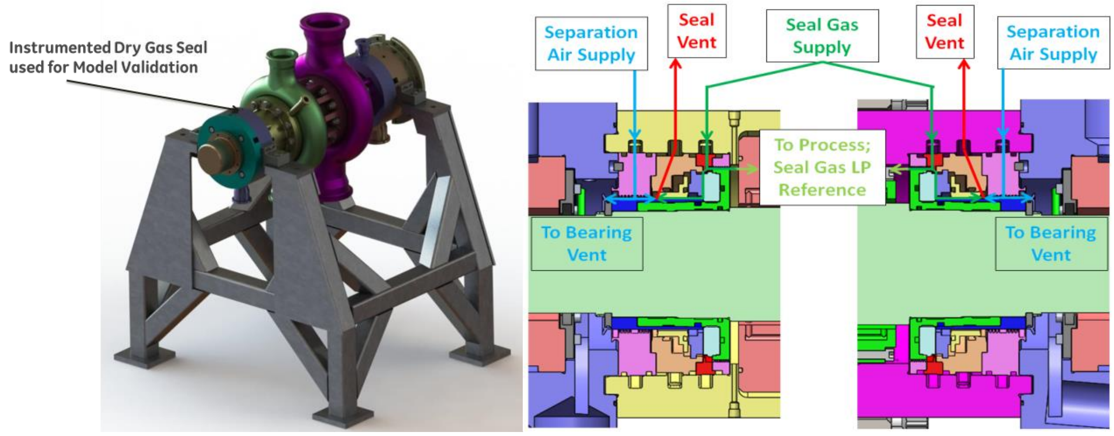

Figure 3: (left) 10MWe sCO2 turbine developed by GE & SWRI under Sunshot program. (right) Dry gas seal flow system used in this turbine.

4. Hybrid Gas Bearing Performance Model

Authors have presented a case for using HGB in a sCO2 turbine in [15]. There a comparison between the layouts of a 10MWe sCO2 expander rotor supported on oil film bearings and the one supported on hybrid gas bearing is presented. Although the rotor is very short in length considering the output power of the machine, the ratio of length over average diameter of the rotor is relatively high. This ratio indicates that the rotor supported on two oil film bearings is a much flexible rotor that is prone to rotordynamic instabilities. Incorporating HGB in this architecture eliminates the need for additional seals and thermal management schemes that would have been otherwise necessary to protect the oil lubricated bearing. The paper summarizes the improvements that can be achieved in the design of sCO2 turbine rotor by using HGB, namely.

In HGB, the turbine operating fluid itself creates the hydrodynamic film that supports the turbine rotor. In addition, there are ports in the hydrodynamic pads that bring in high pressure sCO2 at the center of the pad to provide additional hydrostatic pressure. The multi-scale coupled physics performance prediction model for HGB developed by authors is described in detail in [15]. Figure 4(a) shows the geometry of HGB, a representative FE mesh and the boundary conditions for the model. The model has two steps: 1) Fluid-structural interaction model of the gas film between the rotor and the bearing 2) 3D FE model of HGB assembly with B.Cs obtained from results of step # 1. In the first step, for the steady state solution, the goal is to find the rotor eccentricity that would achieve a force balance between the weight of the rotor and the opposing hydrodynamic / hydrostatic forces. As the rotor starts to spin, a hydrodynamic wedge is created and the rotor is displaced from its centered location to an eccentric location inside the bearing. The hydrodynamic pressure field and consequently the reaction forces of the bearing depend on this eccentric location (e_x, e_y) and is obtained by solving compressible Reynolds equation.

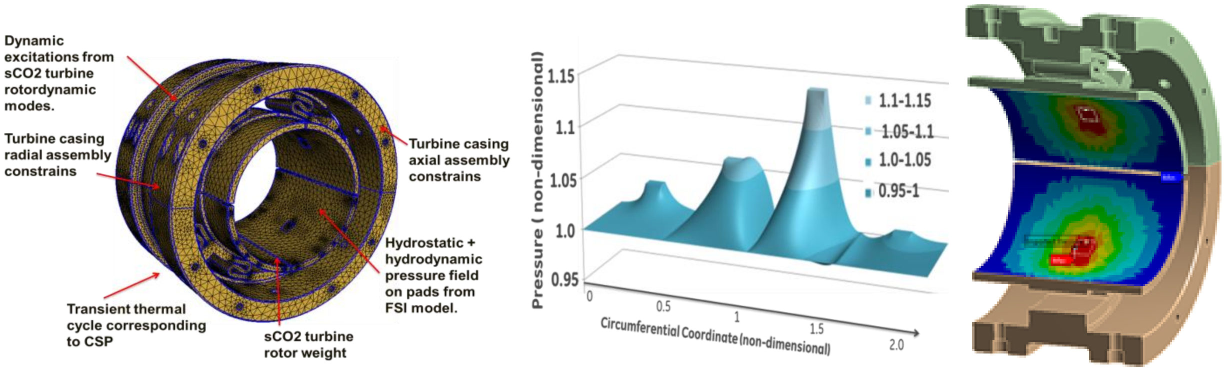

(a) (b) (c)

Figure 4: (a) HGB geometry, FE mesh and the boundary conditions for the HGB performance model. (b) Pressure distribution on HGB pads (hydrostatic + hydrodynamic) obtained from fluid-structure interaction algorithm. (c) Pressure distribution in thin sCO2 film of HGB mapped onto the hydrodynamic pads of HGB for 3D fluid-structure-thermal interaction model.

Having found the steady state pressure distribution and having established a static equilibrium, the next step is to perturb the rotor with a small motion around its eccentric center. The purpose of this step is to characterize the change of the pressure distribution and reaction forces for a small motion around the static equilibrium. The perturbation takes the form of a harmonic orbit with small magnitude and an excitation frequency. Figure 4 (b) shows the static pressure on one of the bearing pads during sCO2 turbine operation. The static pressure field is a combination of both the hydrostatic component generated by the hydrostatic supply pressure coming through the ports on the bearing pad and the hydrodynamic component generated by the spinning rotor. Comparing the film pressure distributions and film thickness results for HGB in sCO2 vs in air operation indicated that for sCO2 with higher density and viscosity than air, minimum film thickness increases as the load that can be carried by HGB without having to ride at very small clearances. Similarly enhanced hydrodynamic effect in sCO2 due to higher viscosity were seen in the pressure profile of pad 2. The pressure in the unloaded pads (1 & 4) is larger in sCO2 due to the larger density of CO2 than typically seen in Air. Effect of rotor speed on direct stiffness K_xx and K_yy of HGB were also computed. The direct stiffness in the vertical direction (direction of rotor weight) K_xx increases with the speed as expected, however the stiffness in horizontal direction K_yy is seen to reduce with increasing speed at a larger rate. This is most likely due to the rotation of the loaded pads about the pivot point, which changes their eccentricity with respect to the rotor preferentially in the X direction compared to Y direction. As the Reynolds number in the sCO2 film between rotor and the pads is much larger than that in the corresponding air film, it is expected that the greater differences will be found between HGB operation in sCO2 and that in air by properly accounting for the turbulence effects in the thin film. Figure 4 (c) shows the pressure distribution in thin sCO2 film of HGB mapped onto the hydrodynamic pads of HGB for 3D fluid-structure-thermal interaction model (step # 2 as described earlier). This 3D FE model that includes all the boundary conditions shown in Fig. 4(a) is then solved to obtain the steady state and transient stress-strain states in the HGB assembly during its operation in the sCO2 turbine. The results serve as the input to the 3D fracture mechanics and life prediction model described in section 7.

Figure 5 shows the HGB test rig (a) and the results for validation (b) of fluid-structure interaction and 3D assembly FE models of HGB using sub-scale test data in air. It shows the comparison of model predictions for strain states in S-springs under various loading conditions with that obtained from test data and confirms that the model is able to accurately capture stress-strain states in the HGB assembly with a very fine resolution under various static and dynamic loading conditions. S-springs of HGB were identified as one of the life limiting sub-components of HGB and ability to predict the finely resolved stress states in these springs arising from fluid-structure-thermal interaction was established as a surrogate for the validation of the multi-scale coupled physics model.

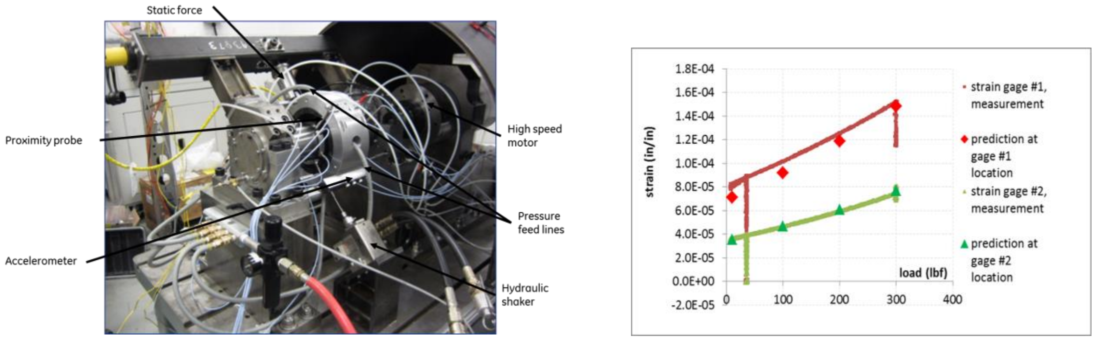

(a) (b)

Figure 5: (a) HGB pressurized rotordynamics test rig used for model validation. (b) Comparison of model predictions for strain in the S-springs of HGB against the experimental data.

5. Phase Transition, 2 Phase Flow and Heat Transport Model

To study phase change and thermal transport characteristics of CO2, a mathematical model for predicting multi-phase fluid flow and heat transport in CO2 is developed. A set of coupled partial differential equations governing phase boundary, surface tension, conduction and convection and moving interfaces between liquid and vapor phases are solved simultaneously. A novel method that describes the transport of phase field variable is incorporated. In addition to the application of studying condensation of CO2 in DGS, another application of this model is in the design of optimal heat exchangers for sCO2 turbomachines. To test the mathematical model, the phase transition during boiling of liquid CO2 due to heat flux from the bottom surface is simulated. Results for time evolution of phase change of CO2 are shown in Fig. 6(a) (Blue = liquid CO2 phase Red= vapor CO2 phase). Three distinct regimes characterize boiling induced by a heated surface: nucleate, transition, and film boiling. The boiling regime depends on the excess temperature (difference between temperature of the solid surface and the saturation temperature of the liquid) and the magnitude of the applied heat flux to the surface.

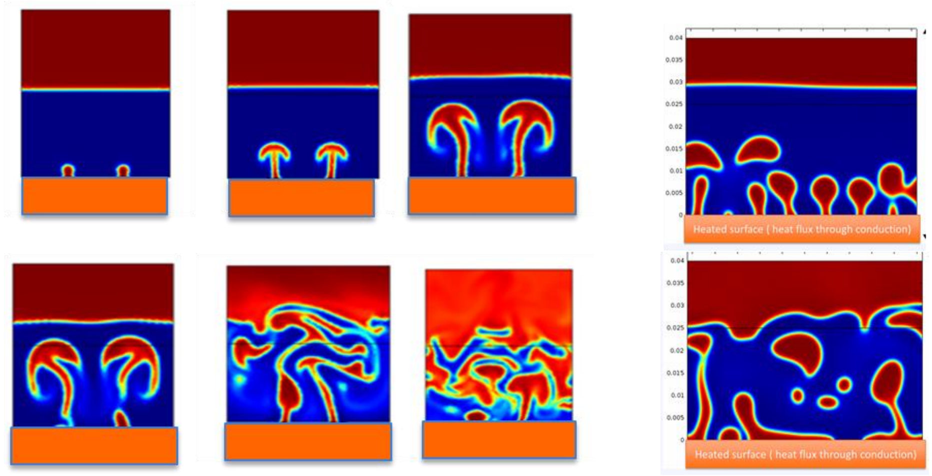

(a) (b)

Figure 6: (a) Model predictions for time evolution of phase transition and the 2-phase flow in CO2 initiated by nucleate boiling phenomenon. Heat flux from the solid surface at the bottom triggers the phase transition. (Blue = liquid CO2 phase. Red = vapor CO2 phase). (b) Transition from nucleate boiling (top) to film boiling (bottom). During film boiling the vapor CO2 blanket covers the metal surface and inhibits the heat flux from metal to CO2 , hence creating local hot spots with extreme high temperature.

In the nucleate boiling regime nucleation sites separate and expand due to mass transfer from the liquid phase to the vapor phase. The bubbles begin to rise due to buoyancy forces and merge with other isolated bubbles to form jets. Because the detaching bubbles are quickly replaced by liquid, the effective thermal conductivity of the fluid layer close to surface is high. This means that even though the applied heat flux is very high, the excess temperature remains low. At this point liquid can still rapidly replace the vapor produced, in effect continuously wetting the surface. This behavior changes when the regime changes to transition and then film boiling (Fig. 6(b)). To sustain film boiling, the excess temperature and applied heat flux must be greater than the Leidenfrost point. In the film boiling regime, layer of vapor CO2 continuously insulates the hot surface from the liquid which hinders the heat transport from solid surface to the liquid. It is also marked with periodic shedding of vapor bubbles from the vapor/liquid interface. One interesting thing to note is that is, unlike water boiling, once the vapor columns are formed they quickly create enough turbulence and mixing to transform the entire liquid CO2 into the vapor phase. During film boiling the vapor CO2 blanket covers the metal surface and inhibits the heat flux from metal to CO2 , hence creating local hot spots with extreme high temperatures. Such local hot spots can cause serious oxidation and corrosion of metal surface, in turn initiating micro-cracks that can reduce the life of the component. Surface roughness created by this corrosion also affects the performance of components like HGB and DGS that rely on extremely fine surface finish. Authors have presented the results for effect on performance due to surface finish degradation arising from sCO2 corrosion elsewhere [16].

6. Experiments to Characterize LCF Life and Fracture Mechanics of Ni base Superalloys in sCO2

6.1 High Pressure, High Temperature sCO2 LCF Tests:

A novel experimental setup (Fig. 7(a)) is developed to measure the low cycle fatigue life of Ni base superalloys in high pressure (> 200 bar), high temperature (> 550 C) sCO2 environment. Test rig consists of a 20 kip servo-hydraulic test frame, equipped with an induction heating unit and a pressure vessel capable of converting liquid CO_2 to supercritical CO_2. A novel hollow bar specimen design is used to flow high pressure, high temperature sCO2 internally through the specimen. As load is applied to the specimen, the extensometer measures the displacement between these two rods and reports the strain in the rod. A feedback control loop is used to maintain the sCO2 temperature and pressure through the specimen at desired test conditions through the test period (which can be as long as a month for low strain tests due high number of cycles to failure).

Fig. 7 (d) shows the fracture plane of a sample specimen tested in sCO2 after it completed its LCF campaign. It shows the typical thumbnail pattern observed on the ID that is typically associated with the crack initiation and growth in LCF tests. This indicates that the specimen indeed failed naturally on the ID where it was exposed to the sCO2 environment. It is generally assumed in the fatigue fracture theory that the in the absence of any environmental effects, the probability distribution of cracks initiating on ID vs those originating on the OD would be approximately equal (no significant preferentiality). Hence if the cracks consistently initiate on the surface which is exposed to sCO2 during the LCF test, then it can be hypothesized that the chemical kinetics between sCO2 and the alloy are playing a role in preferential crack initiation on that exposed surface. Also the reduction in the number of cycles to failure when the specimen is exposed to high pressure, high temperature sCO2 would be the quantifiable measure of effect of sCO2 on fatigue life of the alloy. Assessing the validity of this hypothesis is the objective for this test camping.

Figure 7(b) schematically illustrates the cases of the most favorably oriented grains located on the surface of the fatigue specimen. The section is perpendicular to the specimen surface and the slip plane is at 45° from the loading direction. When dislocations within the slip bands accumulate at the surface of the specimen or at the grain boundary, stress concentrator are generated which favors the nucleation of cracks. Because the slip bands are crystallographic, and thus planar, crack initiation by slip band cracking leads to a facet as illustrated in Fig.7 (e). The first two stages of crack propagation during fatigue testing are illustrated in Fig.7 (c). During stage I, The crack tends to follow crystallographic planes, but changes direction at discontinuities, such as grain boundaries. Facets are generally observed close to the surface because of the extrusion/intrusion defects that slip bands leaves at the surface of the specimens during straining (see Fig. 7(b)). In stage II, crack growth is governed by linear elastic fracture mechanics and the rate depends on the stress intensity factor at the crack tip. The cyclic opening and closing of the crack leads to blunting of the crack tip which leaves striations on the fractured surface. Such striations can be observed in the experimental result of Fig. 11(f) surrounding the facet area.

SEM image in Fig.7(e) shows how the crack initiated during stage I of fatigue fracture in the specimens while the Fig. 7(f) shows a facet which corresponds to slip-plane cracking within a grain. A slip band crack is expected to nucleate in coarser grains which have a high value of cyclic shear stress resolved from the applied stress on the slip plane in the slip direction. In FCC material (like IN718) the 8 {111} slip planes and 12 {112} slip directions are commonly represented by the octahedron. The resolved shear stress on each grain is calculated by the Schmidt factor:

$$m=\cos(\theta)\cos(\lambda)$$

Where θ and λ are the angles between the stress axis and the slip plane normal and slip direction. Under a uniaxial stress, the resolved shear stress becomes maximum when the normal of the slip plane and the slip direction are inclined at 45° to the stress axis.

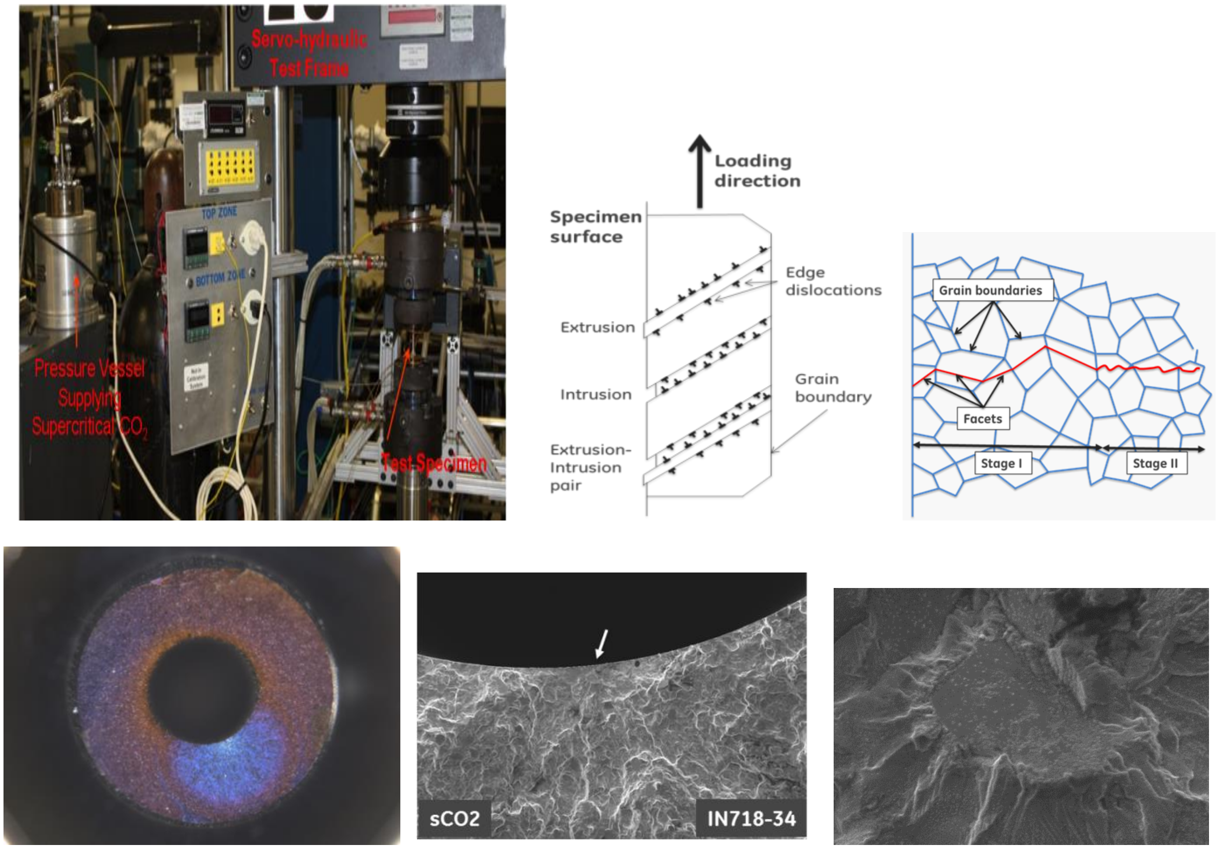

Figure 7: (a) Experimental setup to characterize LCF life of Ni base superalloys in pressurized high temperature sCO2 environment. (b) Schematic of dislocation motion in the most favorably orientated grains and the formation of extrusion and intrusion types of defects by dislocation accumulation [50]. (c) Schematic representation of the crack initiation from surface grains. (d)Fracture plane of the specimen subjected to LCF test in sCO2 after 60,000 cycles. Thumbnail pattern shows that the crack was naturally initiated on the ID where it was exposed to sCO2. (e) SEM image of the crack initiation site. (f) facetted grain showing slip plane cracking within the grain.

Decreasing the amount of strain increases the number of cycles to failure and thus increases the time allowed for any corrosion kinetics to take place. For each strain condition, a baseline is established by determining the LCF life of the new hollow specimen geometry in air. It allows normalizing the debit observed due to the sample geometry (i.e. debit purely from hollow geometry). Tests in air and sCO2 at strain levels from 0.4% to 0.7% are being conducted and the number of cycles to failure as a function of strain level, pressure and frequency of loading are measured.

LCF data (limited data) from the tests conducted so far both in the sCO2 environment and in Air environment (for establishing baseline) is plotted as the S-N curve in Fig. 8. The alternating stress at 0.7% and 0.5% strain is 90 ksi and 63 ksi, respectively. In air, as expected, fatigue life increases when strain amplitude (or alternating stress) decreases. At 90 ksi (or 0.7% strain) both air and sCO2 environment have similar fatigue life which indicates that sCO2 does not significant effect on fatigue crack initiation under such high strain condition, as it does not get enough time to chemically interact with the material under such high stress levels. The upcoming tests are being performed at lower alternating stresses in order to increase the time of exposure of the material to the environment and allow any corrosion/oxidation to take place. Additional tests are also planned to test the “hold time effect” on the LCF life of IN718 (such effect has been observed for other alloys in Air and has been presented in literature [17, 18]).

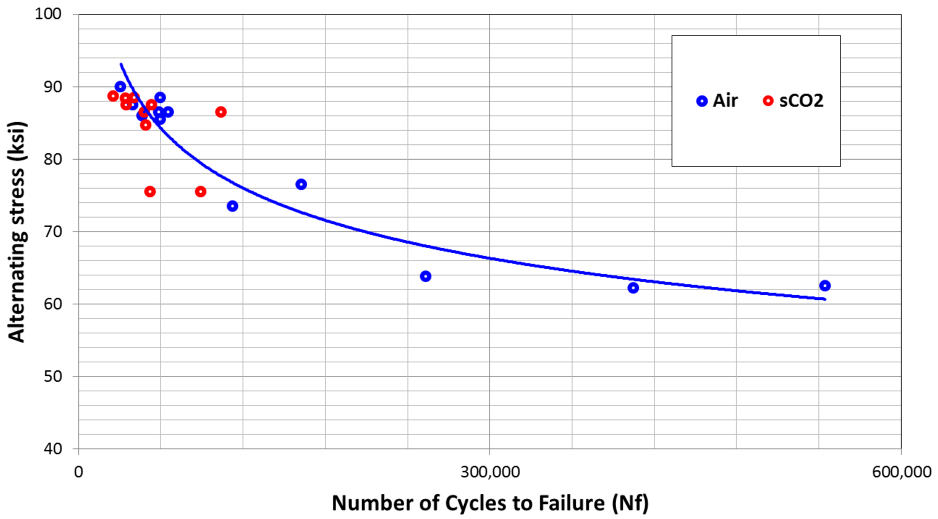

Figure 8: Mean values of the number of cycles to failure for IN718 under LCF loading in air and in sCO2 (based on tests completed so far).

6.2 <u>Experimental Investigation of 3D Crack Propagation using High Energy X-Ray Tomography</u>:

In an effort to capture the effect of the sCO2 environment on In718, electro-discharge machining is being utilized to create notches along the inner bore of the hollow specimen (Fig. 9). The notches act as stress concentrators and increase the probability of crack nucleation (followed by the crack propagation process) at these specific sites which are exposed to sCO2. Also, damage monitoring is more efficient since the location is known a priori to the test procedure.

Fig. 9(b) shows the methodology for crack growth rate measurement and how it serves as input the 3D fracture mechanics and crack propagation models.

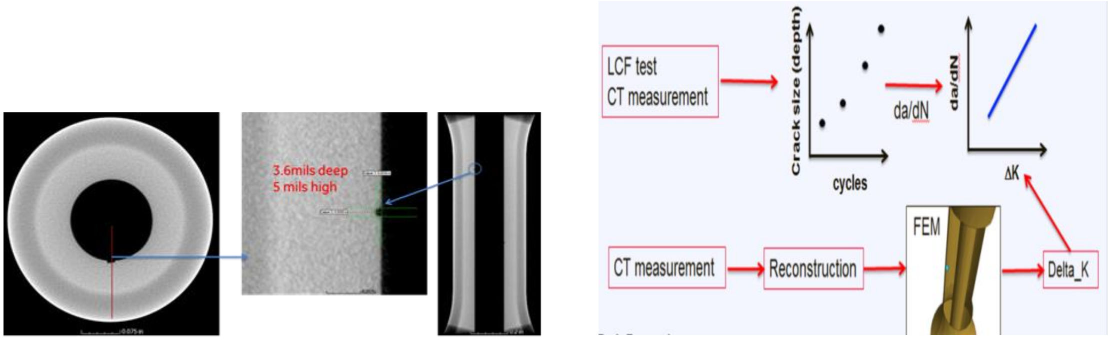

(a) (b)

Figure 9: (a) CT images of the notch locations introduced using EDM. Resolution carried in the measurements: 15 micron/pixel. (b) Methodology of crack growth rate measurements and how it serves as input the 3D fracture mechanics and crack propagation models.

Since *In-situ* monitoring of accumulation of damage (crack growth) inside the hollow specimen during the sCO2 LCF test is not possible, a high energy X-Ray Computer Tomography (non-destructive evaluation) technique is used to track crack growth inside the LCF test specimens at regular intervals during testing. For this purpose, authors used European Synchrotron Research Facility (ESRF), one of the highest energy X-ray sources in the world available for this type of measurement (electrons accelerated to 6GeV). ESRF provides one of the best imaging capabilities in the world, with energy range (>200 keV) and resolution (< 1 mm), suited to capture features (micro-cracks) of interest.

High energy X-ray computer tomography (CT) performed provides volumetric damage information at different time points of the fatigue test procedure. Once scanned, the specimen continued the sCO2 LCF test procedure and a follow-up X-Ray tomography procedures disclosed the evolution of the damage in time. It reveals evolution of population (size, density) of micro cracks in time and how they transform into long crack behavior leading to final failure. Effect of oxidation and sCO2 corrosion in initiating micro-pits if any also becomes apparent.

The first scan was conducted on a specimen that sustained 15000 LCF cycles at sCO2 exposure of P=200 bar T=550 C and strain = 0.7%. The CT measurement was conducted with a FOV of 12.9 x 3.5 mm and resolution of 3.4 microns. A representative cross-section of the scanned volume is shown in Figure 10(a). The conclusion was that no damage was identified in this measurement. Specimen then continued sCO2 LCF testing until 23000 cycles at which point it was again sent for CT scans. Location, shape and size of the crack in the gage section observed after 23000 cycles is shown in Fig. 10 (b, c) while (d) is the X-ray tomography slice of the same specimen after 23000 cycles and shows the cracks evolved. Fig. 10 (e)-(g) show the shape and size of the crack in various planes located at different z heights along the specimen gage section and (h) the side view of these z locations in the specimen.

Hence Fig. 10 (e)–(h) clearly show how the above technique captures micro-crack evolution in 3 dimensions without destroying the specimen (without which it would not have been possible to track crack growth) with a resolution of as little as 0.9 micron to help calibrate and validate the physics based 3D fracture mechanics models with high accuracy.

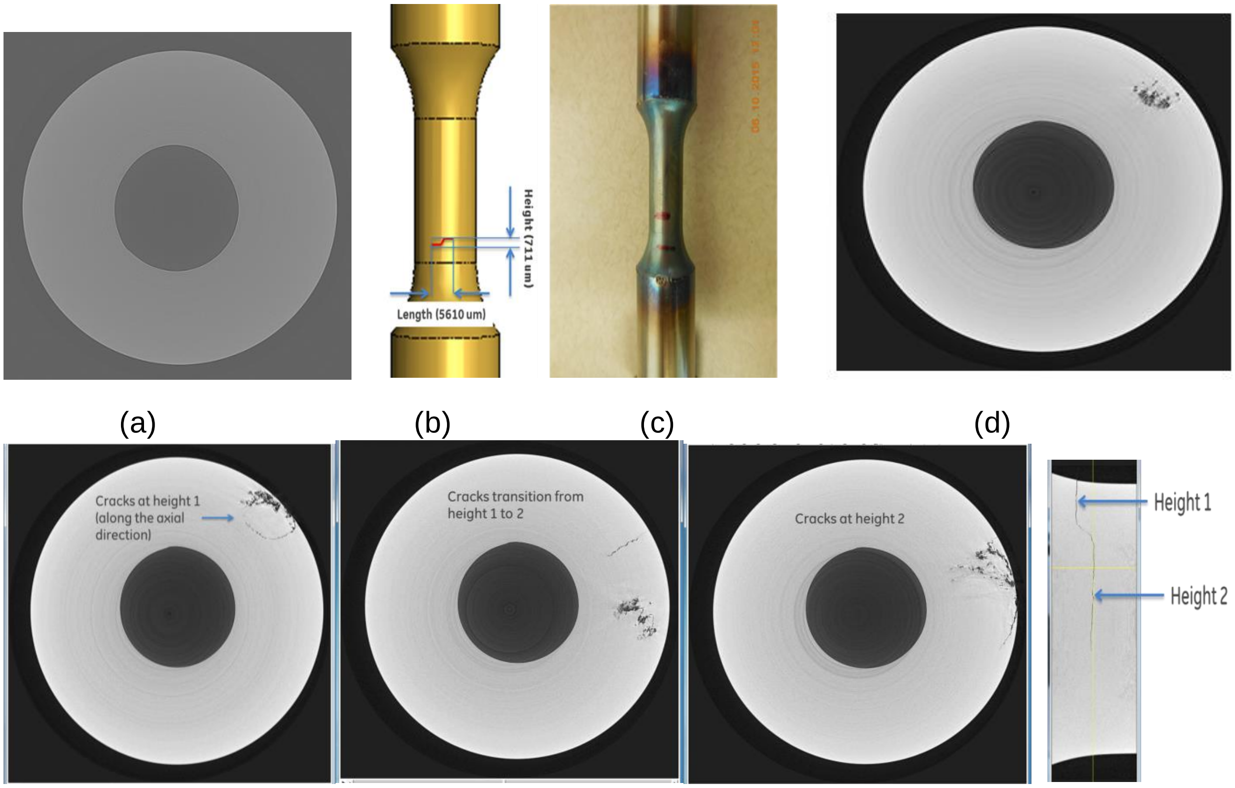

(a) (b) (c) (d)

(e) (f) (g) (h)

Figure 10: (a) A sample X-ray tomography slice in the gage section of test specimen after 15000 cycles of sCO2 LCF testing. No damage was detected in thousands of such 3.4 micron resolution slices stacked up along Z axis. (b, c) Location, shape and size of the crack in the gage section observed optically after 23000 cycles of sCO2 LCF test. (d) X-ray tomography slice of the same specimen as in (a) but after 23000 cycles shows the crack evolved. (e) shape and size of crack at z location of height 1 (f) transition of the crack from z=height 1 to z=height 2 (g) shape and size of crack at height 2 (h) z locations of height1 and height 2 in the side view of the specimen.

6.3 <u>Digital Reconstruction of 3D Crack Morphology from the X-Ray Tomography Image Stacks:</u>

The post-processed images from the X-Ray Tomography measurements, constituting a stack, were cleaned, cropped, aligned, and segmented into a three dimensional morphology using python and DREAM.3D (for stacking and aligning the images and segmenting the pixels related to vacuous space (i.e. a crack) into a three-dimensional model). Isolating the crack from noise and other artifacts is easy to do with the naked eye, but difficult for computers. Consequently, before segmentation, each image had to be “cleaned” with intelligent image processing algorithms. The processed images were then fed into DREAM.3D for alignment and segmenting image pixels that belong to crack from those that do not belong to crack. After application of the segmentation filter, the resulting three-dimensional model in point-cloud form was output into a VTK file as a rectilinear (structured) grid. Figure 11 shows visualization of digitally reconstructed cracks that are then used to calibrate and validate the 3D fracture mechanics model (discussed next) results in a quantitative manner.

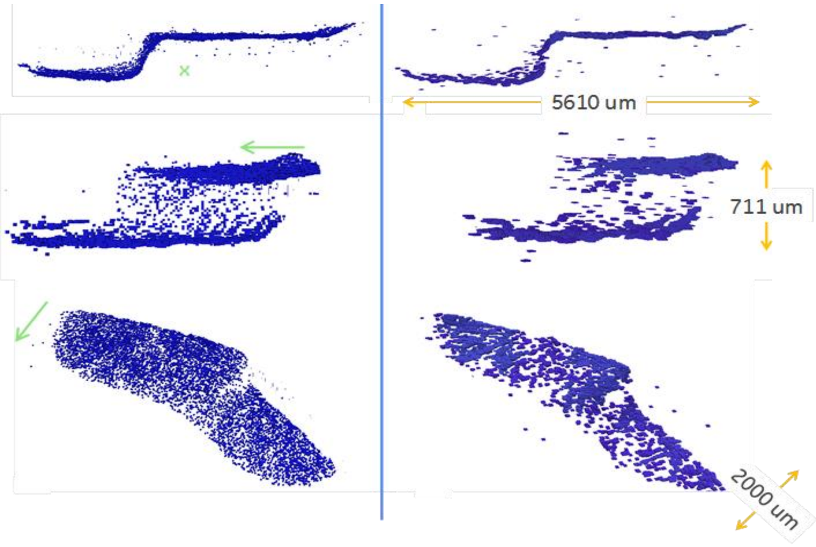

Figure 11: Crack reconstructed digitally in 3D using X-Ray tomography data. The green arrows demarcate orientation (wherein the arrows are always pointing into the specimen). The orange arrows demarcate the lengths of the cracks along different directions.

7. 3D Fracture Mechanics and Life Prediction Model

7.1 Crack Propagation Model:

Having obtained the stress-strain states in HGB under the transient loading mission of 10 MWe sCO2 turbo expander as discussed in section 4 earlier, this 3D distribution of stress-strain states was used as input to the 3D fracture mechanics and life prediction model. Crack propagation life of HGB was assessed using GE's internal fracture mechanics tool 3DFAS [9-11].

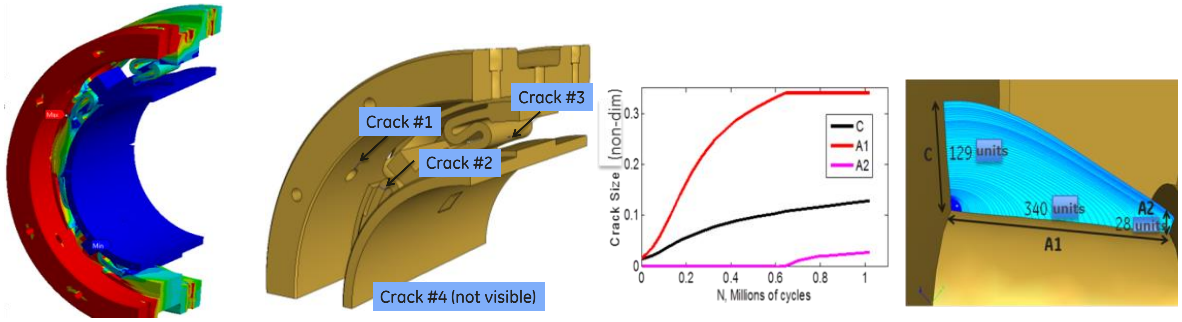

(a) (b) (c) (d)

Figure 12: Crack propagation results for various cracks in HGB operating in 10 MWe sCO2 turbine with a CSP mission cycle. (a) Stress distribution in HGB during sCO2 turbine mission cycle (b) 4 different cracks with their expected locations predicted from 3D FE model. (c) Crack size parameters as a function of number of loading cycles for crack # (d) Results for propagation of crack # 2.

3D fracture mechanics and crack propagation life assessment for HGB is conducted using 3DFAS code. Based on the stress-strain distributions in HGB assembly in a sCO2 turbine during CSP mission cycle obtained from performance predictions discussed earlier, three crack locations were chosen where the first principal stresses were high. Figure 12 (a) shows the sample stress distribution in HGB at one of the time stamps. Figure 12(b) shows the location of the 4 cracks expected from the results of 3D fluid-thermal-structural FE model discussed earlier. Crack #1 is a corner crack that is located near the bolt hole. Crack #2 is also a corner crack that is located in the S-shaped spring perpendicular to the cross section. Crack #3 is a surface crack in the S-shaped spring located in the center. The initial crack size was fixed to a depth of 15 mils for all the cracks. The crack size evolution for crack # 1 and #2 is shown in Figure 12 (c) & (d) respectively. Crack #2 grew faster than the other cracks and reached the thickness of the S-shaped spring therefore limiting the life of the bearing to 1 million cycles for the simulated loading conditions (start-up/shut-down). Crack #1 begins as a corner crack that grows asymmetrically and reaches bolt seat when it becomes an edge crack. Figure also shows the crack growth rate and crack length as a function of number of LCF cycles. From this study, an estimate on the service life of HGB in a typical MW scale sCO2 turbine can be obtained.

7.2 Model for Crack Initiation Life under Corrosive Environment:

The total life of a component in an environment consists of two parts: 1) crack initiation life (time required for first micro-cracks to initiate in the component) and 2) crack propagation life (time required for initiated cracks to propagate to cause final failure of the component). In the previous section we described the crack propagation model. In this section we describe our efforts to develop an analytical model for predicting the crack initiation life of IN718 alloy under LCF in a corrosive environment of supercritical CO2 at elevated temperatures. The crack initiation life model to be developed should be generic for a wide range of temperatures, metal-CO2 chemical kinetics, strain levels and duration of exposure to the corrosive environment. Since under the current program, the sCO2 LCF tests are still underway and hold time tests are yet to commence, GE’s prior experimental data for IN718 tests in air was used to calibrate the Arrhenius-type temperature and hold time dependent Crack Initiation Life Prediction model. The purpose here is to use the development of the model and explain the basic philosophy. Once entire sCO2 LCF tests are completed, the model will be calibrated against this sCO2 test data. Another constraint on the life model development is to use an Arrhenius type of temperature dependence (*exp (Q/RT)*) in the analytical model such that an activation energy term for the relevant gas-metal combination could be used. In such model, the activation energy Q that is specific to the combination of IN718 and sCO2 will be used. This activation energy Q is calculated from long term sCO2 corrosion tests performed under this program. The results of these experiments are already published [16] and hence are not repeated here.

Authors used existing LCF data for IN718 in air for a wide range of temperatures and the hold times to calibrate and validate the crack initiation model. Some of the data are plotted in Fig. 13. As the hold time increases, the LCF curve moves towards the left leading to lower life. This can be attributed to the corrosive, undesirable action of the environment on the surface of the material, an oxide layer build-up in this case. Another trend that is not explicitly seen in these series of plots is the effect of temperature on life. Hence LCF data for wide range of temperatures are plotted in Fig. 13 (right) for a constant hold time. For higher strain ranges, the higher temperatures have an undesirable effect on life, while at lower strain ranges the effect is not very significant.

Another important aspect of the data is the shape of the LCF curve. In Fig. 13, the strain range and cycles to initiation are plotted in log-log scale and the LCF curve is not straight. The reason for this non-linear behavior is due to LCF/HCF transition. The steeper slope captures the LCF life, while the shallow slope captures the HCF life. Since the strain range-life data exists for a wide range of strain-levels, temperature and hold times, the data does not fall into either pure LCF or HCF category. These type of LCF curve is best described by the Coffin-Manson Relation given below:

$$\Delta\varepsilon = \frac{\sigma_f'}{E}\left(2N_f\right)^b + \varepsilon_f'\left(2N_f\right)^c \qquad \text{(Eq.1)}$$

While the first term corresponds to elastic stresses and strains (HCF), the second term corresponds to plastic stress and strain (LCF). Life model development requires non-linear curve fitting of the data.

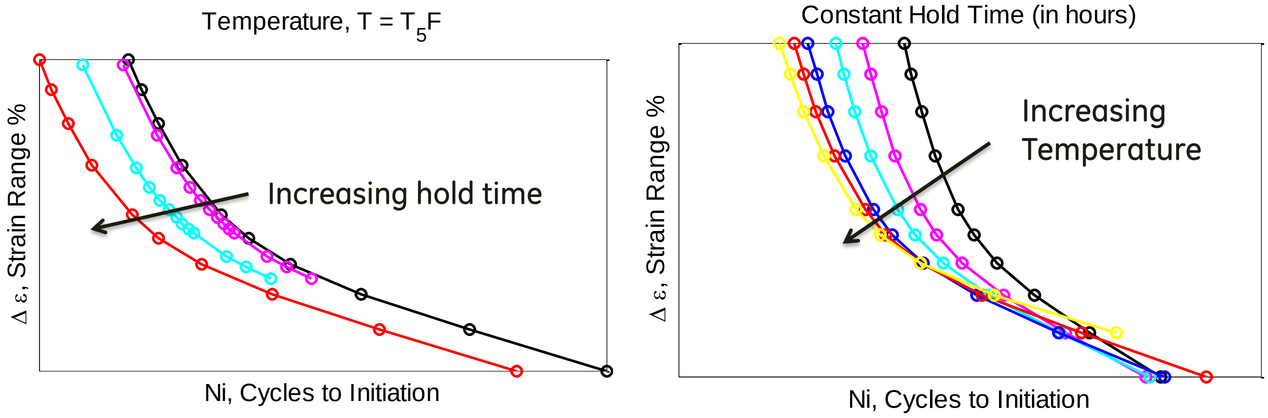

Figure 13: (a) LCF Data (strain range versus life) for various hold times at a constant temperature (T5 F).(b) LCF data showing effect of temperature for constant hold time.

Taking into Account the Effect of Chemical Kinetics between sCO2 and the Metal:

Various LCF life models as a function of strain range exist in the literature [19, 20]. The most commonly used model is the Coffin Manson Life equation given in Eq. (2) with two terms. However, the Arrhenius type chemical kinetics term (*exp (Q/RT))* ,does not appear explicitly in this life model. Antolovich *et.al* [17, 18] developed a crack initiation life model based on the oxide layer build-up and stress level in the material. Authors have modified this model with a Bayesian Hybrid Probabilistic approach to identify the correct constants and exponents of this model while still retaining the term describing inherent chemical kinetics between sCO2 and the alloy (Eq. 4). In this equation the variable Q captures the Activation Energy between sCO2-metal pair, which is already found experimentally by the authors and is reported elsewhere [16]. In this model, the oxide layer builds up uniformly on the surface everywhere except where the grain boundaries intersect with the surface. In these locations, an oxide spike is observed that is much deeper than the uniform scaling of oxide layers. These oxide spikes are the source of crack formation. The crack initiation occurs at a critical combination of oxide spike depth and stress (expressed in terms of plastic strain). The total structural life (N_f) can be split as the sum of two independent processes of failure; elastic (N_F) and plastic (N_i):

$$\frac{1}{N_f} = \frac{1}{N_F} + \frac{1}{N_i} \tag{2}$$

where,

$$N_F = \frac{B}{(\sigma_{max})^{-p}} \tag{3}$$

$$N_i = A\left(\Delta\varepsilon_p\right)^{-m} exp\left(\frac{Q}{RT}\right)\left(\frac{1}{\nu} + t_h\right)^{-n} \tag{4}$$

An important feature of this model is that it resembles the Coffin Manson equation and it also contains the chemical kinetics term (*exp (Q/RT)*) explicitly in the life equation. The crack initiation life predictions from the above model are compared with the raw data as shown in Fig. 14. A point along the 45 degree line corresponds to good prediction.

P.K. Wright [] claims that Antolovich model overemphasizes time dependence effect especially unstressed exposure. To overcome these challenges, authors are developing a more advanced model to capture effect of chemical kinetics on crack initiation life.

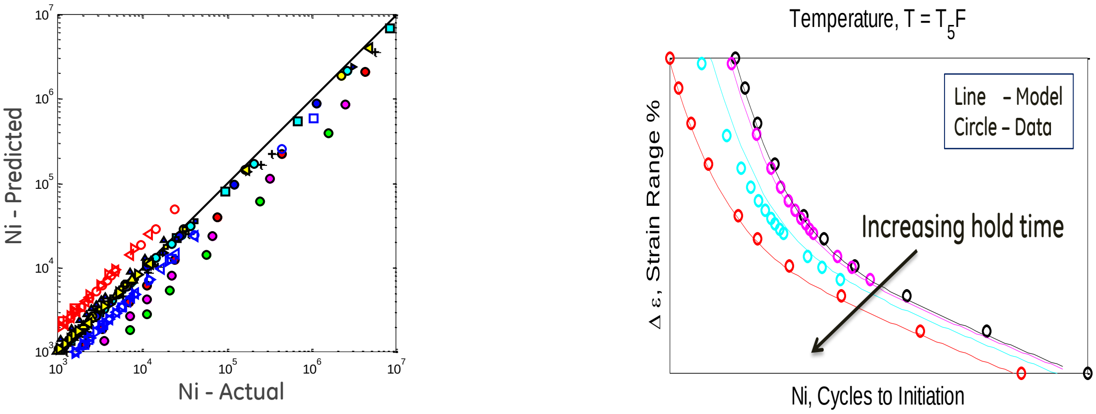

Figure 14: (Left) Comparison of model predictions with the experimental data for In718 in air. (Right) Comparison of model predictions with the experimental data at a specific temperature of T_5 F (exact temperature not revealed due to proprietary nature of the prior data used) . The solid lines represent the model while the circles represent raw data.

8. BHM Probabilistic Framework

Bayesian Hybrid Probabilistic Model (BHM) was used extensively to quantify uncertainty in physics based performance and life prediction models of DGS and HGB, to calibrate those models and to validate the models.

Probabilistic assessment of the life prediction model was done by performing crack propagation simulations on a hollow bar subject to uncertainties on material properties and crack sizes.

Uncertainty Quantification and Its Effect on Crack Propagation Rate:

As uncertainties in fatigue properties of materials are deemed to dominate other uncertainties such as the ones on applied load spectra, the material parameter uncertainties on crack propagation are quantified and propagated in formulating the crack growth of a probabilistic model. We also account for uncertainties on initial crack size and final crack size at which catastrophic failure occurs.

Hypothesis in this task is that the statistical distribution of crack propagation life predicted by GE's 3D fracture mechanics code is lower than the LCF measurement data due to the fact that, the simulation assumes an initial crack of a given size while in the actual test the corrosive environment / micro-structure mechanisms have to first initiate the crack and therefore there is additional life that is not accounted for in the model. Development of the crack initiation life model was addressed in previous section, and this model is integrated into the BHM probabilistic framework.

Probabilistic simulation of crack propagation is conducted by performing forward uncertainty quantification (UQ) analysis using a BHM model that is built with the numerical results of GE's in-house 3DFAS code at Design of Experiment (DOE) samples.

Uncertainties on the initial and final crack (depth) sizes are modeled independently by taking into account the uncertainty bounds on those parameters. Bound of initial sizes is estimated given that the long crack behavior starts when the crack is 5-10 times larger than average grain size (about 10 microns=0.4 mils). The width of an initial crack is assumed to be same as the depth, and the propagation life is determined when the depth of a crack reaches to a final size during 3DFAS simulation.

Uncertainties of the two propagation parameters C and n are modeled based on assumption that they are independent of those of crack sizes.

The number of cycles to advance a crack with a given increment "da" corresponding to a stress intensity factor is computed based on a formulation proposed by Paris and Erdogan [53],

$$\frac{da}{dN} = C\Delta K^n \qquad (10)$$

In general, uncertainties of the two propagation parameters C and n are obtained by processing a multiple data sets of crack growth experiments and characterized using upper and lower bounds.

An average material property curve of IN718 in sCO2 is obtained in which C and n are obtained by performing a regression analysis of raw experimental data. A bivariate normal distribution was found to meet the criteria with a mean value of C_mean and n_mean. The coefficient of variations of C and n were found to be 24.2% and 2.56% and their correlation coefficient was found to be -0.90. The bivariate normal distribution is illustrated using Monte Carlo samples in Fig. 15(a). Fig. 15(b) shows the scatters of simulated data points corresponding to the input parameter uncertainties and it is noted that the majority of data point scatters are contained within 2X uncertainty band (in dotted lines).

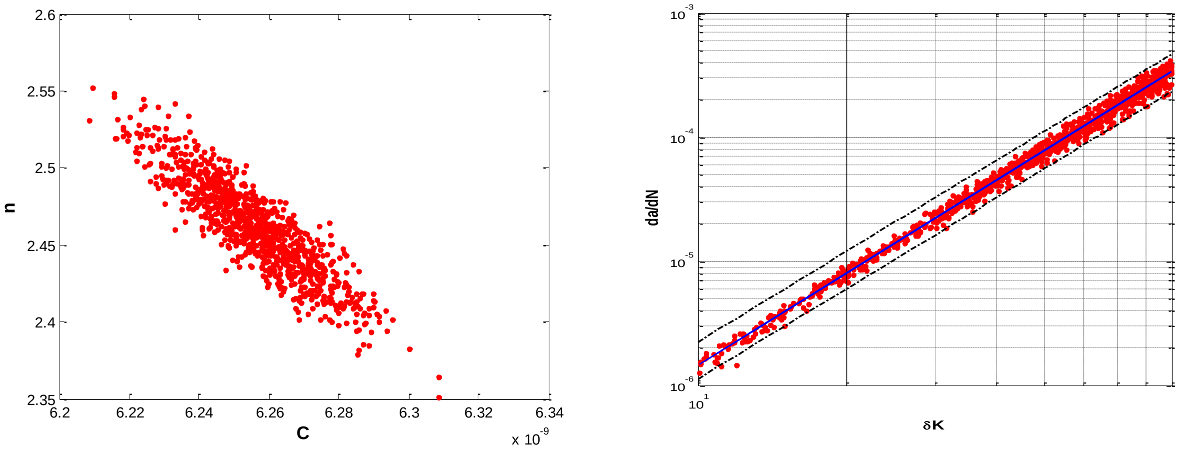

(a) (b)

Figure 15: Uncertainties of material parameters and corresponding uncertainties in crack propagation data. (a) Monte Carlo samples of bivariate normal distribution for C and n. (b) Scatters of simulated data points for crack propagation.

BHM model is then built to simulate the high-fidelity crack propagation model that uses GE's in-house 3DFAS code. 50 DOE samples of four input parameters are generated using optimal Latin-hypercube (OLH) sampling technique as shown in Figure 16(a). 3DFAS code is used to compute the number of cycles to propagate an initial crack to a final size of each sample.

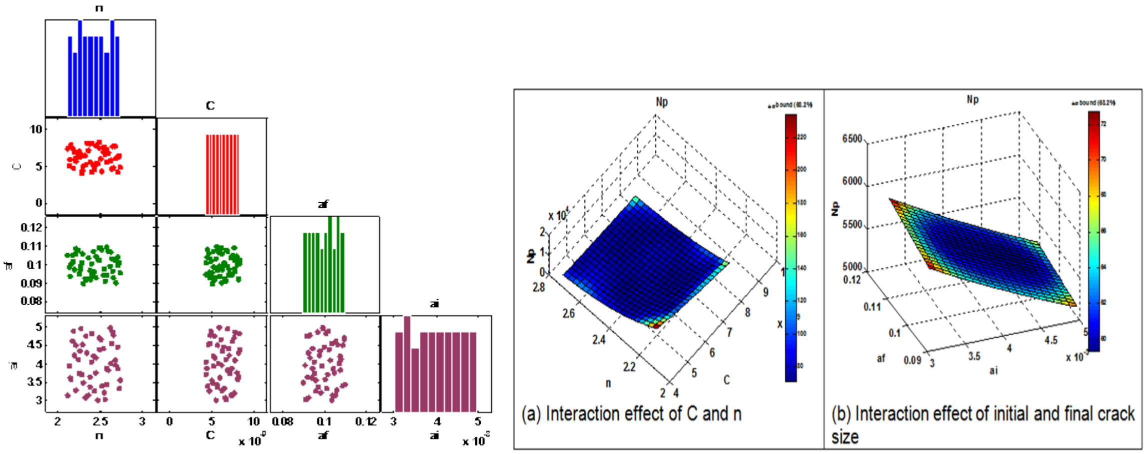

(a) (b)

Figure 16: (a) DOE samples of four input parameters. (b) Three dimensional plots of the BHM model for Np and their uncertainties. It is noted that the uncertainties are relatively large in regions where DOE samples are not available. Np response is monotonically decreasing as C and n increase, and its dependence on crack size parameters becomes evident.

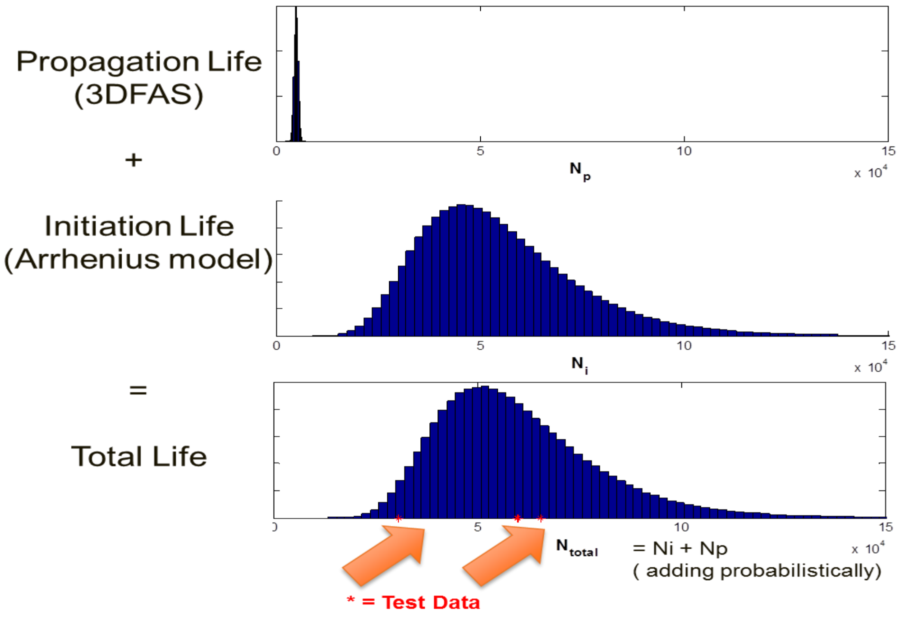

Figure 17: Distribution of crack initiation life, crack propagation life and total life of IN718 in sCO2 obtained from BHM probabilistic model are plotted along with the corresponding test data (red dots).

After developing the BHM model, the probabilistic crack propagation cycle of a hollow bar subject to uncertainties is estimated by performing forward UQ analysis. UQ analysis quantifies uncertainties of Np by propagating 100,000 random samples each of which is made up of two crack size and two material variables from uniform and bivariate normal distributions, respectively. Probabilistic prediction of propagation cycle, Np, is illustrated using a histogram of 100,000 simulation results. The mean and median of the distribution are 5033 and 5010 cycles with a standard deviation of 493 cycles. When we add the crack initiation life (e.g. ~60,000, 100,000 or 200,000 cycles depending on the strain level) to the above crack propagation life, then the model matches the total life of the specimen observed experimentally. This is shown schematically in Fig. 17 where the first probability distribution (top) is the actual distribution calculated using physics based crack propagation model (Np), while the second distribution (middle) is the distribution for crack initiation life (Ni) of IN718 in air based on prior literature (this will be replaced by the actual model predictions for crack initiation in sCO2 once more calibration data becomes available through additional LCF tests in sCO2). When the two distributions are superimposed, we get the probabilistic distribution for total life of the component (bottom). Sample experimental data is also shown using red dots which is encompassed by the life PDFs obtained from the model.

9. CONCLUSIONS

Multi-scale coupled physics models to predict dynamic performance of HGB and DGS are developed. The models try to capture sCO2 specific phenomena like sonic transitions, possibility of phase change, flow induced and rotordynamic instabilities and large perturbations in apparent heat transfer coefficients. The output of performance model is fed into 3D fracture mechanics based life prediction framework. Test campaigns to characterize corrosion of Nickel base super alloys in sCO2 environment are conducted and chemical kinetics models are built. LCF behavior of Ni base super alloys in high pressure, high temperature sCO2 is also being investigated using a novel experimental setup. Bayesian hybrid probabilistic models are developed to quantify uncertainty in multi-physics models and to validate models with statistical confidence. This strongly coupled performance and life prediction framework is a valuable tool to design a wide variety of sCO2 turbomachinery components and heat exchangers, analyze their performance in supercritical and trans-critical mission cycles and predict their life for long term durability of sCO2 turbomachines.

10. REFERENCES

[1] Kalra C., et. al., “Development of High Efficiency Hot Gas Turbo-Expander for Optimized CSP Supercritical CO2 Power Block Operation, The 4th International Symposium on Supercritical CO2 Power Cycles, Pittsburgh, Pennsylvania, 2014.

[2] San Andrés, Luis. "Hybrid flexure pivot-tilting pad gas bearings: analysis and experimental validation." Journal of tribology 128.3 (2006): 551-558.

[3] Fangcheng Xu, Yi Sun, Zhansheng Liu, Yu Wang, Guanghui Zhang, and Ning Xu, “The Effect of Coulomb Friction in Foil Structure on the Static and Dynamic Performance of Bump Foil Journal Bearings.” ASME Turbo Expo 2014: Turbine Technical Conference and Exposition. American Society of Mechanical Engineers, 2014.

[4] Heshmat, H. "Advancements in the performance of aerodynamic foil journal bearings: high speed and load capability." Journal of Tribology 116.2 (1994): 287-294

[5] Ertas, Bugra Han. "Compliant hybrid gas journal bearing using integral wire mesh dampers." U.S. Patent No. 8,083,413. 27 Dec. 2011.

[6] Ertas, Bugra H. "Compliant hybrid journal bearings using integral wire mesh dampers." Journal of Engineering for Gas Turbines and Power 131.2 (2009): 022503.

[7] Delgado , Adolfo “Experimental Identification of Dynamic Force Coefficients for a 110 mm Compliantly Damped Hybrid Gas Bearing” , ASME Turbo Expo 2014: Turbine Technical Conference and Exposition. American Society of Mechanical Engineers, 2014.

[8] Standard, A. P. I. "684, 2005,“." Tutorial on Rotordynamics: Lateral Critical, Unbalance Response, Stability, Train Torsional and Rotor Balancing,” Second Edition, American Petroleum Institute, Washington, DC.

[9] A. Loghin, 2013, "Integrated Computational Materials Engineering at General Electric", *TMS 2013 Keynote*, San Antonio, TX..

[10] A. Loghin, U. Ozkan, A.C. Kaya, J. LeMonds,R. McClain, D. Decesare, S.Akkaram, J. Laflen, 2012, "3DFAS: Framework for Conducting 3D Crack Growth Simulation," *Propulsion - Safety and Affordable Readiness*, Florida.

[11] O. Klass, R. Nastassia, M. Beall, A. Loghin, J. LeMonds, J. Laflen, “Robust Tools for crack insertion and propagation”, NAFEMS World Congress, Boston, MA, May 23-26, 2011.

[12] Kumar, N., Subramaniyan, A.K., Wang, L., "Improving high-dimensional physics models through Bayesian calibration with uncertain data," June 11-15, 2012, GT2012-69058, ASME TurboExpo 2012,Copenhagen, Denmark.

[13] Makino, T., Morohoshi, S., and Taniguchi, S., "Application of average flow model to thin film gas lubrication," Journal of Tribology, 115, 185-190 (1993).

[14] Thatte A. et.al., "Coupled Physics Performance Prediction and Risk Assessment for Dry Gas Seal Operating in MW-Scale Supercritical CO2 Turbine" , Proceedings of ASME Turbo Expo 2016, June 13 – 17, 2016, Seoul, South Korea, GT2016-57670.

[15] Thatte A., et.al., "Performance and Life Characteristics of Hybrid Gas Bearing in a 10 MW Supercritical CO2 Turbine", Proceedings of ASME Turbo Expo 2016, June 13 – 17, 2016, Seoul, South Korea, GT2016-57695.

[16] Dheeradhada V., Thatte A. et.al., 2015, "Corrosion of Supercritical CO2 Turbomachinery

Components", EPRI International Conference on Corrosion in Power Plants, San Diego, CA.

[17] S.D. Antolovich, S. Liu, R. Baur, "Low cycle fatigue behavior of Rene 80 at elevated temperature", Metullrgical Transactions A, 12A, pp.473-481, 1981.

[18] S.D. Antolovich, N. Jayaraman, "The effect of microstructure on the fatigue behavior of Ni based superalloys", Proceedings of the 27th Sagamore Army Materials Research, pp. 119-144, 1980.

[19] P. Paris, F. Erdogan, A critical analysis of crack propagation laws, Journal of Basic Engineering, 85, pp. 528-534, 1963.

[20] Norman E. Dowling, Mechanical Behavior of Materials, 4th Edition, Pearson Publishing, 2012.

Acknowledgement: This material is based upon work supported by the Department of Energy under Award Number DE-EE0006345.

Authors would like to thank Dr. Adolfo Delgado of GE Global Research for his help in providing the test data for HGB operation in air and for providing insights into the HGB performance characteristics. Authors also thank Dr. Tim Allison and Dr. Jeff Moore of Southwest Research Institute for providing rotordynamic data on Sunshot turbine rotor and the DGS flow loop architecture for Sunshot turbine.

Author Biographies:

Dr. Azam Thatte is a Lead Research Engineer at GE Global Research Center in Niskayuna, NY. He received Ph.D. in Mechanical Engineering from Georgia Tech in 2010. His research interests include multi-scale multi-physics modeling, fluid-structure interaction, aircraft engine design, turbomachinery flows, hydrodynamic film riding sealing and gas bearing technology. Currently Dr. Thatte is the Principal Investigator of a large U.S. DOE research program on developing coupled-physics performance and life prediction models and material models for supercritical CO2 turbomachines. He has developed novel experimental methods to characterize thermodynamics of phase transition in CO2 and to study effect of chemical kinetics of CO2 on 3D fracture mechanics in superalloys. He has authored more than 30 journal & peer reviewed conference publications including one in Nature. He has also filed 12 patent applications.

Adrian Loghin joined General Electric Global Research Center (GRC) in 2001 as a Mechanical Engineer with expertise in Fracture Mechanics and Fatigue. He received his Ph.D. from Clemson University, South Carolina in the area of Nonlinear Fracture Mechanics. He published several peer review papers and GRC reports. Adrian is one of the developers of 3DFAS (Three Dimensional Fracture Mechanics).

Dr. Etienne Martin is a Lead Materials Scientist at GE Global Research Center in Niskayuna, NY. He received Ph.D. in Materials Engineering from McGill University in 2010. His research interests include processing, characterization and mechanical testing of materials for air craft engine and gas turbines.

Voramon Dheeradhada is a materials scientist at GE Global Research Center in Niskayuna, NY. She received her Ph.D. from Purdue University in Materials Science and Engineering in 2005 and has been with GE since 2005. Her research focuses on high temperature structural materials especially in the area of environmental attack. Her prior work includes (but not limited to) bond coat development, high temperature degradation behavior of metallic alloys and bond coat, diffusion and thermodynamic modeling, and microstructure-property relationship.

Dr. Youngwon Shin is a Senior Research Engineer at GE Global Research Center in Niskayuna, NY. He received Ph.D. in Aeronautics and Astronautics Engineering from Univ. of Washington in Seattle. His research interests include Bayesian modeling, uncertainty quantification, structural analysis is, reliability and risk analysis, design optimization, fracture mechanics and fatigue crack growth analysis, and statistical modeling and analysis to solve complex problems in engineering.

Dr. Balajee Ananthasayanam is a Mechanical Research Engineer at GE Global Research in Niskayuna, NY since 2010. His research at GE is focused on developing, validating and applying state-of-the-art physics-based life-prediction methodologies to high-value components in power generation and propulsion, oil & gas equipment with a goal of improving design robustness & optimizing service utilization. He received masters and doctorate degrees in Mechanical Engineering from Clemson University. His research interests includes fracture mechanics, fatigue, creep and viscoelasticity, mechanical behavior of high temperature super-alloys, glass and polymers.